I&EC research
Industrial & Engineering Chemistry Research

pubs.acs.org/IECR

Article

Residence Time Distribution Characterization and Proof-of-Concept of a Novel Stacked 7-Stage Continuous Crystallizer Cascade with Diaphragm-Driven Slurry Transfer

Published as part of Industrial & Engineering Chemistry Research special issue "Marco Mazzotti Festschrift".

Giovanni Aprile, Ajinkya V. Pandit, Jody Albertazzi, Thomas Vetter, Robert Viano, Lorenzo Milani, Andrea Adamo, Allan S. Myerson, and Torsten Stelzer*

Cite This: *Ind. Eng. Chem. Res.* 2024, 63, 18199−18211

Read Online

ACCESS | Metrics & More | Article Recommendations | Supporting Information

ABSTRACT: Process developers in the pharmaceutical industry lack readily deployable, standardized, off-the-shelf continuous crystallizers (<100 mL), abiding the low material requirements of early stage product development. This study evaluates a novel continuous tower crystallizer (TWC), hosting a series of seven vertically stacked mixed suspension mixed product removal crystallizers (MSMPRCs, 80 mL total volume) enabled by an innovative diaphragm driven slurry transfer, which eliminates known transfer line issues in MSMPRC cascades. Residence time distribution measurements using the model compound glycine demonstrate ideal mixing for both liquid (homogeneous) and solid (heterogeneous) phases (particle < 100 μm, slurry density < 22.8%). A comparison with the tank in series model reveals nonideal mixing for particles >300 μm. Finally, a proof-of-concept continuous antisolvent crystallization of glycine demonstrates the TWC's capability to produce high-quality crystals continuously, proving its functional and robust operation.

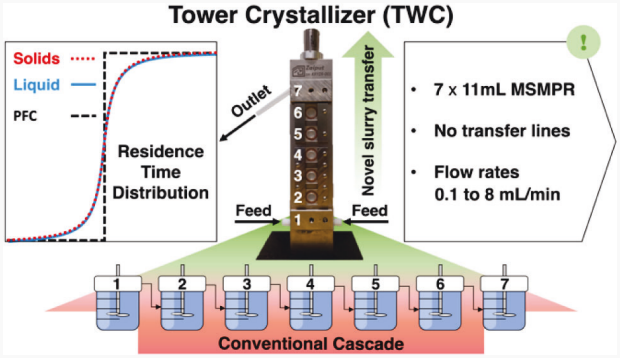

1. INTRODUCTION

Crystallization is an essential unit operation and often the most robust and cost-effective approach for purification and separation of fine chemicals and active pharmaceutical ingredients (APIs).[1−5] About 90% of all APIs (organic molecules) require crystallization with the desired purity, physical attributes (e.g., particle size, morphology), and physicochemical properties (e.g., dissolution, bioavailability) associated with the solid form (e.g., polymorph, solvate, salt) that alter the performance of downstream processes and the API.[1,2,5,6] While continuous API molecule generation (flow chemistry)[7−20] and formulation[21−24] have already reached commercial pharmaceutical manufacturing readiness, API crystallization is still mostly conducted in batch processes.[3,4,12,25,26] This represents a major obstacle for continuous, end-to-end pharmaceutical manufacturing, which requires continuously operating crystallizers as the missing link.[4]

Though continuous crystallizers are used in large-scale, high-volume productions (kg to tonnes per hour) in the agrochemical, commodity, dairy, and food industries for decades, well-characterized continuous crystallizers with robust and predictable performance in much smaller pharmaceutical manufacturing scales remain a key challenge.[3,4] Specifically, miniaturized crystallizers (<100 mL) are needed to accommodate the small production rates (g per day) of potent and precious APIs at the laboratory scale in early research and process development (R&D).[4] The two most common pharmaceutical crystallizer designs are[1−3] (i) the continuous stirred-tank reactor or mixed suspension, mixed product removal crystallizer (MSMPRC), including single and multistage[27] and (ii) the tubular type plug flow crystallizer (PFC)[27−29] including segmented flow[30,31] and oscillatory baffled crystallizers.[32,33] While the MSMPRC represents the workhorse for pharmaceutical manufacturing with custom- and purpose-built crystallizers, the other designs mostly remain in the academic literature with limited industrial applications because of isssues such as fouling, particle settling, and/or down-scaling (e.g., oscillatory baffled crystallizer).[1−4,31] To date, there is no satisfying off-the-shelf technological solution

Received: June 7, 2024
Revised: September 20, 2024
Accepted: September 23, 2024
Published: October 9, 2024

https://doi.org/10.1021/acs.iecr.4c02153
Ind. Eng. Chem. Res. 2024, 63, 18199−18211

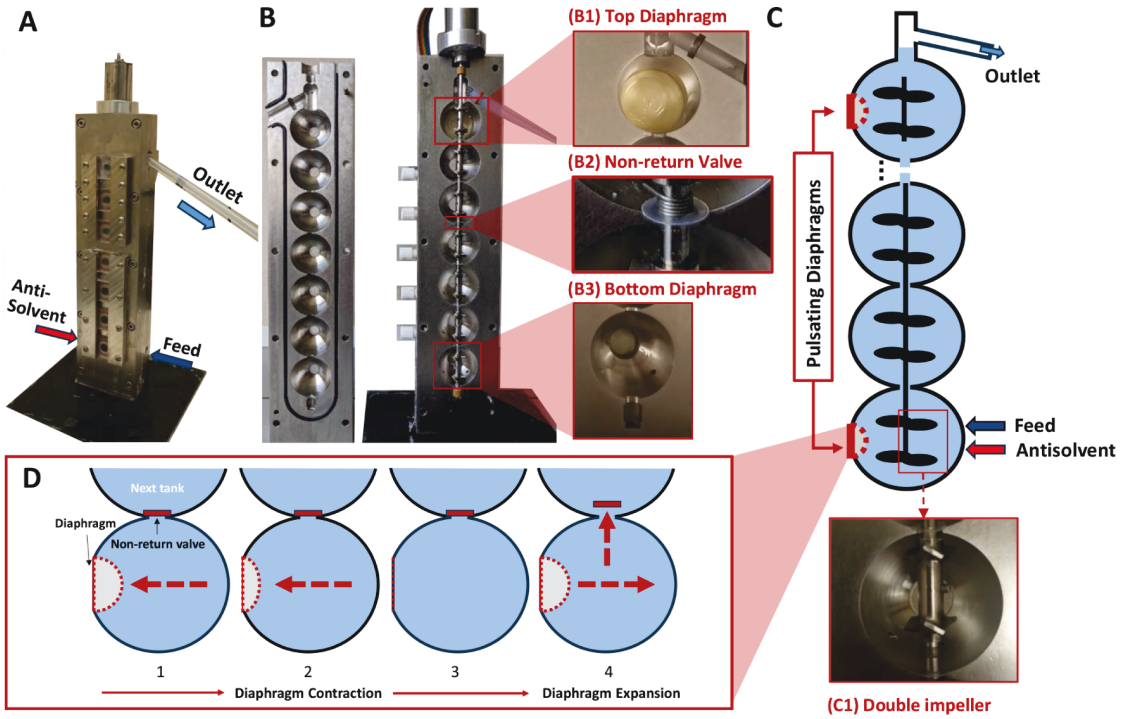

Figure 1. A) Fully assembled tower crystallizer (TWC) with inspection windows. B) Disassembled TWC with detailed views of the top and bottom diaphragms (B1 and B3), and nonreturn valve (B2). C) Schematic representation of the SSC cross-section and detailed view of the double impeller (C1). D) Schematic illustration of the diaphragm pulsation cycle and nonreturn valve movement (an impeller shaft has been removed to simplify the illustration).

that addresses the needs for robust and miniaturized continuous crystallizers (<100 mL) that can also reduce the API consumption during R&D.[4]

Generally, the MSMPRC is preferred for low conversions, long residence times, and high slurry density. The PFC is favored for higher conversions with short residence times and low slurry density at any residence time due to the settling of crystals at low Reynolds numbers.[1−3,31] On the other hand, the MSMPRC provides a robust operation with intensive mechanical mixing that reduces fouling and settling but suffers from broader residence time distribution (RTD) compared to the PFC, which potentially widens the crystal size distribution (CSD) and leads to nonuniform product quality. To approach plug flow characteristics, MSMPRCs can be connected in series, known as a cascade, enabling narrower RTDs and CSDs while increasing yield.[1,2] Mathematical simulation models based on population balance equations demonstrate that a cascade approaches the equivalent of a PFC with an increasing number of MSMPRCs[34] with less tendency toward fouling/clogging when the slurry transfer lines between the MSMPRCs are cleared.[31,35] However, the slurry transfer in such small crystallizers is challenging, leading to continuous flow rates as small as 0.17 mL/min reported at the outlet of a 30 mL MSMPRC,[36] which results in low withdrawal velocities and failure of isokinetic withdrawal.[2,35,37] To date, intermittent (periodic) withdrawal at very high flow rates is commonly employed as a mitigation strategy[1,2] using (i) partial vacuum applied in a product hold tank,[12,26,35,37,38] (ii) peristaltic or centrifugal pumps,[36,39−41] and (iii) positive pressure in the headspace.[42] The latter allows one to maintain a small overall footprint of the MSMPRC, including slurry transfer equipment, which for the former two is generally much greater than the size of the MSMPRC.[1] Thus, continuous crystallizers with novel slurry transfer mechanisms are demanded by the industry.[4]

The work presented here addresses this unmet need for a continuous and scalable (scale-down/up) crystallizer[4] by characterizing a novel stacked cascade crystallizer prototype developed by Zaiput Flow Technologies for the first time, called a tower crystallizer (TWC). The TWC consists of a series of seven miniaturized MSMPRCs (11.4 mL per MSMPRC) that mimic plug flow characteristics while alleviating all issues related to mL-scale MSMPRC cascades via a novel diaphragm-driven slurry transfer. Further equipment details are provided in Section 2.

In this proof-of-principle study, RTD experiments were conducted to provide experimental insights into the macromixing dynamics of the TWC.[2,5,27,43] Based on these RTD experiments, it is possible to identify and quantify nonideal flow patterns, such as dead volume, bypassing, short-circuiting, or classification.[44] Preventing classification phenomena is of utmost importance in any continuous crystallizer,[42,45] because particles with longer residence times are exposed to growth conditions for longer times and hence grow to larger sizes than their counterparts exposed to shorter residence times. In the extreme case where particles accumulate, they would grow indefinitely over time.[46] To better understand the transport of solids (crystals) inside the novel TWC, the presented study measures the RTDs for both the liquid phase (L-RTD) and the solid phase (S-RTDs). To the best of the authors' knowledge, the number of publications reporting on S-RTD characterization of continuous crystallization processes is scarce and mostly focused on the tubular type[47−52] but are lacking for stirred tank type designs[48] similar to the TWC. The results of the RTD experiments were also compared with the theoretical RTD of an ideal MSMPRC cascade and a plug flow

https://doi.org/10.1021/acs.iecr.4c02153
Ind. Eng. Chem. Res. 2024, 63, 18199−18211

crystallizer.[2,5,27,43] Finally, a proof-of-concept continuous antisolvent crystallization of glycine from a water−ethanol mixture was conducted in the TWC prototype.

Essentially, the results of this investigation will contribute to the design optimization of the TWC and serve as input for further experimental designs aimed at fully characterizing the novel continuous crystallizer.

2. MATERIALS AND METHODS

2.1. Materials. Glycine (HPLC grade) was acquired from Sigma-Aldrich (Merck KGaA, Germany). Ethanol (ACS grade) was supplied by Koptec (Decon Laboratories, Inc., USA). Deionized water (18.20 MΩ/cm, pH = 7.03, mV = −42.0) was obtained using a Barnstead Micropure Water Purification System (Thermo Fisher Scientific Inc., USA). All materials were used "as received" without purification.

2.2. Tower Crystallizer (TWC). The TWC prototype, designed by Zaiput Flow Technologies (Zaiput), is comprised of two frames machined out of 316L stainless steel (Figure 1A,B). Upon assembly, these frames create a sequence of seven spherical tanks, each with a volume of 11.4 mL, arranged in a stacked configuration (Figure 1C). The tanks are interconnected by short sections (length of 1 mm, internal diameter [ID] of 5 mm). Each tank is equipped with two customized down-pumping pitched-blade impellers (3 blades, 11 mm diameter), mounted on a common shaft (3 mm outer diameter [OD]) providing rotational and axial mixing.[53] All agitation parts are machined in 316L stainless steel, except the impellers, which are 3D printed. The stirrer shaft is connected to an overhead motor control that ensures mechanical mixing, making each tank a functional MSMPRC (Figure 1C). The feed solution and antisolvent are added into the cascade at the bottom (first) MSMPRC through two inlet ports (UNF 1/4−28) using two positive displacement pumps (VICI, M50). Though not employed in the presented proof-of-principle study, the TWC enables antisolvent addition in each of the tanks, allowing for tuning the concentration profile and, thus, the quality of the crystallized compound.[2,28]

2.2.1. Diaphragm-Driven Slurry Transfer. Two diaphragms are strategically positioned in the first and seventh MSMPRCs of the cascade. The bottom diaphragm operates on a pulsating cycle (Figure 1D), systematically expanding and reducing the volume of the first MSMPRC. During the contraction phase, the diaphragm synchronizes its velocity with the flow rate of the feed and antisolvent streams to retain the incoming material in the first tank and to prevent backflow from the second tank until it reaches maximum capacity (Figure 1D, step 3). Upon completing the contraction cycle, a rapid expansion reduces the working volume in the tank, pushing the material upward (Figure 1D, step 4). Due to the incompressibility of liquids and the absence of a free surface (no headspace) in each tank, the upward transport of material occurs simultaneously throughout the entire cascade.

The top tank of the TWC (7th MSMPRC) is not equipped with inlet ports and, distinct from the other tanks, operates with a headspace volume. Its primary role is to facilitate the slurry ejection through an outlet tubing (1/4′ OD, 1/8′ ID, and fluorinated ethylene propylene (FEP)). The slurry is ejected in the form of slugs, preventing settling, via a movable diaphragm, which operates on a moving pattern different from that of the bottom one (detailed above). This diaphragm quickly expands to allow the ejection of a defined amount every time the desired volume is ready to be ejected.

2.2.2. Non-Return Valves for Backflow Prevention. To prevent backflow between the tanks, FEP disc-shaped sheets (7 mm diameter) are placed above each interstage clearance (bottom of each tank), held down by a stainless-steel spring positioned on the stirrer shaft (Figure 1, B2). These nonreturn valves allow the material to flow upward into a tank during the step-expansion of the bottom diaphragm, while preventing backflow into the tank below during the diaphragm contraction phase (Figure 1D).

2.3. Experimental Setup for Residence Time Distribution (RTD) Characterization. Both solid (S-RTD) and liquid phase (L-RTD) characterizations were conducted in the experimental setup shown in Figure 2. The setup consisted of

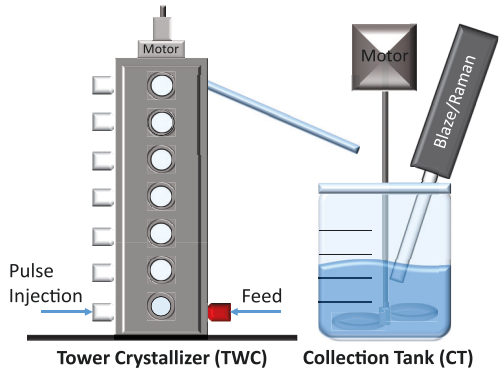

Figure 2. Schematic representation of the experimental setup used for both L- and S-RTD characterization.

the TWC sided by a 1000 mL stirred collection tank (CT). To monitor the cumulative collection of material outflowing from the TWC, process analytical technology probes were immersed in the CT. For the L-RTD experiments, a Hyperflux Pro Plus 785 nm Raman spectrometer (Tornado Spectral Systems, Canada) was immersed in the CT, and for S-RTD, a BlazePlatform Micro probe (Blaze Metrics, USA) was used. Both L-RTD and S-RTD were studied in independent experiments employing the pulse input method, respectively.[45,50]

2.3.1. Liquid RTD (L-RTD) Characterization. Experimental L-RTD (no solids present) curves were determined using an aqueous glycine solution (200 mg/mL) as a liquid tracer monitored by in situ Raman spectroscopy in the CT (Figure 2).[28,45,50] The data recording via Raman spectroscopy is detailed in Section 2.3.3 below. Prior to each experiment, the TWC was prefilled with the carrier (water) from the bottom and stirred at 2000 rpm. The rationale for the stirring rate is provided in Section 4. The CT was also prefilled with 400 mL of water and stirred at 200 rpm using a down-pumping 4-pitched blade impeller (diameter 60 mm). To ensure stabilized hydrodynamic conditions in the TWC prior to the pulse injection, the carrier was continuously fed into the bottom MSMPRC at a flow rate of 5.3 mL/min, corresponding to a mean residence time (RT) of 15 min over the whole MSMPRC cascade. The mean RT (τ) was determined employing eq 1:

$$\tau = \frac{V}{Q} \tag{1}$$

where V represents the working volume of the TWC and Q is the volumetric flow rate of the liquid going into the first tank.

https://doi.org/10.1021/acs.iecr.4c02153
Ind. Eng. Chem. Res. 2024, 63, 18199−18211

After 3 RTs, ∼1 mL of the tracer solution was swiftly injected manually into the bottom MSMPRC through the antisolvent injection port (Figure 2) using a 5 mL Luer-lock syringe (UNF 1/4−28 flat bottom, VWR International). The experiments were conducted in triplicate, each lasting ≥3 RTs (≥45 min), typically sufficient to detect any deviations from plug flow behavior.[50,54] The time of injection was considered time zero ($t = 0$) for the RTD analysis detailed in Section 3. The transfer time between the TWC and the CT was short compared to the mean residence time (<5%) and was thus assumed negligible in the measurements for L-RTD as well as S-RTD detailed in the following.

2.3.2. Solid RTD (S-RTD) Characterization. Similar to the L-RTD characterization, a modified pulse input method was used for the S-RTD at a mean RT of 15 min employing glycine crystals as a solid tracer suspended in the liquid carrier ethanol (antisolvent for glycine).[55] A rationale for the modified pulse input method is given in Section 4. For the approach, ∼1.6 and ∼2.6 g of glycine crystals were added to the first tank of the horizontally disassembled TWC (Figure 1B). These amounts resulted in a theoretical slurry density of 140 and 228 mg/mL, respectively, upon the addition of ethanol in the first MSMPRC. Though slurry density is defined as the mass of solids per unit volume of solution,[5] in this study, the fill volume of ethanol (antisolvent) was not precisely measured. Therefore, the slurry density was calculated assuming that the antisolvent volume equals the volume of the first tank (11.4 mL). Consequently, the reported slurry density is likely smaller than the actual values.

Once the TWC was closed and vertically positioned, tanks 2 to 7 were carefully filled manually from bottom to top with ethanol using a 20 mL syringe with a Luer lock (VWR International, LLC.) connected to the antisolvent injection ports of each tank (Figure 2). Thereafter, the first tank was filled with ethanol at a volumetric flow rate of 5.3 mL/min using a positive displacement pump. After 129 s, corresponding to 11.4 mL of liquid added at this flow rate, the stirrer and diaphragms were activated to start the continuous operation of the TWC ($t = 0$) for the RTD analysis, Section 3). While the S-RTD experiments with 140 mg/mL slurry density were conducted in triplicate, the experiments with 228 mg/mL only in duplicate due to a technical issue.

The cumulative particle counts during the S-RTD experiments were monitored in situ in the CT using the Blaze probe (Figure 2). Details of the data recording are provided in Section 2.3.4. In addition, at the end of each S-RTD, the CT content was vacuum-filtered using a Büchner funnel (Whatman grade 42 ashless filter paper, 55 mm diameter) and dried at 70 °C using an oven at ambient pressure (Yamato, ADP-31). The chosen temperature was below the reported thermal decomposition temperature of glycine over a prolonged time.[56,57] The crystals were weighed every 24 h using an analytical balance (XS104, Mettler Toledo Inc., ±0.1 mg precision) until a constant weight (±0.1 mg) was recorded for at least three consecutive measurements. The comparison between the mass of crystals loaded into the crystallizer and the mass recovered provides a quantitative estimate of settling phenomena or particles trapped in the device.[58] For the assessment of particle size effects on the S-RTD, tracers of three different sizes were obtained by sieving commercial glycine crystals using a Sieve Tester oscillator (model SS-15, Gilson Company Inc.) equipped with sieve mesh sizes of 600, 300, and 100 μm (A.S.T.M. E-11 Specification, VWR).

2.3.3. Raman Spectroscopy. For the L-RTD characterization, the tracer concentration in the CT was monitored by tracking the glycine-characteristic Raman peak at 898 cm^{-1}, following a calibration-free approach (Figures S1 and S2).[59] The raw spectra were collected using a Tornado Raman spectrometer and the software Spectrasoft (version 3.5.0.0) with enabled dark correction and cosmic ray filters employing the following settings: exposure time, 1s; each spectrum averaged over 15 exposures; spectrum collection interval, 1 s. To avoid light interference and background noise, the CT was wrapped in aluminum foil. For further data analysis, the raw data were baseline-corrected with the iterative algorithm Goldindec in the Matlab environment (Version R2023b, The Mathworks, Inc.).[60] To allow comparison with the tank-in-series (TIS) model,[46] the spectra were normalized as reported in Section 3.

2.3.4. Blaze Image-Derived Total Chord Length Monitoring. For the S-RTD characterization, the solid tracer was monitored in situ by tracking the image-derived total chord length counts per second of the particles by using the Blaze probe and the Blaze user interface (Blaze_UI, version 148.04.03). The measurement duration was set to 10 s, recording up to 58 images/s analyzed.[61] Thus, each image-derived chord length distribution (ID-CLD) was based on ∼580 images every 10 s. The image plane was positioned at 40 μm, via the Blaze user interface, which provided the optimal image quality during preliminary experiments. Similar to the L-RTD characterization, the raw trends were normalized (Section 3).

2.4. Continuous Antisolvent Crystallization. Figure 3 depicts the experimental setup for the continuous crystallization using the TWC. The setup is similar to that for the RTD characterization experiment, but the Blaze probe is mounted in a prototype flow cell (Y-flowcell, BlazeMetrics) positioned at the TWC outlet tubing (see also Section S3) to monitor the chord length distribution and counts in-line. The mother liquor concentration was quantitatively assessed via the gravimetric method once per residence time (from the fifth RT) throughout the experiment[62,63] and in triplicate at the end. To minimize the experimental effort for the offline mother liquor concentration measurement, samples were drawn once the in-line monitored signals for the solids stabilized after ∼5 RT, indicating the end of the startup phase.[47] Briefly, three 5 mL slurry samples were drawn using Luer-lock 10 mL syringes and immediately filtered (Whatman Syringe Filter, 0.45 μm, polypropylene membrane, Cytiva). Thereafter, ∼2 mL of the

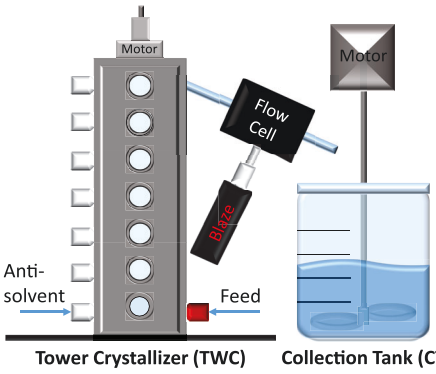

Figure 3. Schematic representation of the experimental apparatus and configuration used for continuous antisolvent crystallization.

https://doi.org/10.1021/acs.iecr.4c02153
Ind. Eng. Chem. Res. 2024, 63, 18199−18211

clear mother liquor was dispensed into preweighed 2 mL HPLC vials. The total weight of the vials maintained at 70 °C under reduced pressure (ADP31, Yamato Scientific American Inc.) was frequently measured using an analytical balance (XS104, Mettler Toledo Inc., ± 0.1 mg precision) until their weight remained unchanged (±1 mg).

Glycine, a fast-growing compound,[47,64] was selected as the model compound to be crystallized from water with ethanol as the antisolvent.[65] Prior to the continuous crystallization experiment conducted at room temperature (~22.0 ± 1.0 °C), all tanks were prefilled with feed solution (200 mg/mL glycine in water) using the feed pump at a flow rate of 4.5 mL/min. Once the solution was visually observed exiting the TWC, the continuous operation was initiated by activating the stirrer, diaphragms, and antisolvent (ethanol) pump immediately. The antisolvent flow rate was set to 0.8 mL/min to maintain, combined with the feed flow rate, an antisolvent volume fraction of 0.15. The choice of these conditions was based on preliminary experiments and should be understood only as an example and not in any way as optimized operating conditions. These flow rates corresponded to a mean RT of 15 min throughout the TWC. Attainment of steady-state conditions was judged based on consistent CLDs observed over at least three consecutive RTs.[37,40,66,67] The experiment was conducted for a duration of ≥10 RTs without clogging.

3. ANALYSIS OF RTD RAW DATA

The pulse input method employed to measure the RTD typically entails monitoring the evolution of the outlet concentration of the tracer over time after an initial injection at the inlet.[46] Therefore, it is common practice to position an appropriate detector directly immersed in the crystallizer[68] or in a flow cell at the effluent,[45] to obtain direct measurements of the RTD function $E(t)$ (eq 2).[46]

$$E(t) = \frac{c(t)}{\int_0^\infty c(t)\mathrm{d}t} \tag{2}$$

Here, $E(t)$ is expressed in its standard form, as the ratio of the tracer concentration in the outlet stream $c(t)$, at a given time t, to the integral of the outlet concentration with time over the course of an RTD experiment. In the study presented here, the concentration detector was immersed in the CT (Figure 2) and not at the outlet stream. Details of the rationale are provided in Section S2. Thus, the tracer will accumulate in the CT over time (for both L-RTDs and S-RTDs) and it is more useful to assess the cumulative distribution function $F(t)$ as expressed by eq 3.[46,69]

$$F(t) = \int_0^t E(t)\mathrm{d}t \tag{3}$$

Substituting eq 2 into eq 3, the relationship between $F(t)$ and the concentration response in a standard pulse trace experiment (measured using a flow cell at the outlet) at any time point t is expressed by eq 4.[46]

$$\int_0^t c(t)\mathrm{d}t = F(t)\int_0^\infty c(t)\mathrm{d}t \tag{4}$$

Since the tracer concentration was measured in the CT and not in the outlet stream, a suitable correction needed to be applied to eq 4 to account for the increasing volume in the CT and thus tracer dilution occurring throughout the experiment to enable the calculation of $F(t)$ from the measured concentration profile in the CT. The time varying concentration of the tracer in the CT, $C_{CT}(t)$, may be expressed as the ratio of the time-varying mass of the tracer accumulated in the CT, $m_{CT}(t)$, and the time-varying volume of the CT, $V_{CT}(t)$, as shown in eq 55.

$$C_{CT}(t) = \frac{m_{CT}(t)}{V_{CT}(t)} \tag{5}$$

Using the tracer concentration in the outlet stream, $c(t)$, and the TWC volumetric flow rate, v, $m_{CT}(t)$ can be calculated using eq 6, while $V_{CT}(t)$ may be expressed as a function of v and the initial CT volume, V_0, shown in eq 7.

$$m_{CT}(t) = \int_0^t vc(t)\mathrm{d}t \tag{6}$$

$$V_{CT}(t) = (V_0 + vt) \tag{7}$$

By substituting eqs 4, 6, and 7 into eq 5, the relationship between $C_{CT}(t)$ and $F(t)$ can be derived (eq 8).

$$C_{CT}(t) = \frac{v}{(V_0 + vt)}F(t)\int_0^\infty c(t)\mathrm{d}t \tag{8}$$

To elucidate the connection between $F(t)$ and $C_{CT}(t)$, eq 8 was rearranged resulting in eq 9.

$$F(t) = \frac{C_{CT}(t)(V_0 + vt)}{v\int_0^\infty c(t)\mathrm{d}t} \tag{9}$$

The term $\int_0^\infty c(t)\mathrm{d}t$ in the denominator of eq 9 equals a constant and hence will not affect the results when raw data are normalized between 0 and 1. Thus, a correction term $(V_0+vt)/v$ is suggested for the CT concentration (liquid or solid) to obtain the cumulative RTD in a conventional sense. The as-obtained tracer trends were then normalized using the maximum values recorded for the Raman intensity of the peak at 898 cm^{-1} for L-RTD[59] and the particle counts for S-RTD. Moreover, since the minimum Raman intensity of the peak at 898 cm^{-1} is not zero, the corresponding normalized value $\overline{x}$ for each data point x of a given experimental RTD was obtained by subtracting the minimum recorded value x_{min} and dividing it by the difference between the maximum x_{max} and minimum x_{min} recorded values (eq 10). A key assumption implicit in this method is that the Raman intensity changes linearly within the tracer concentration range investigated (verified in Figures S1 and S2).

$$\overline{x} = (x - x_{min})/(x_{max} - x_{min}) \tag{10}$$

The normalized cumulative RTD trends were compared against the TIS model (ideal mixing), adapted for seven tanks (n = 7, eq 11):[46]

$$F(t) = \int_0^t \frac{t^{n-1}}{(n-1)!}\left(\frac{n}{\tau}\right)^n \exp\left(-\frac{tn}{\tau}\right)\mathrm{d}t \tag{11}$$

where τ refers to the mean residence time as defined in eq 1. To quantify the goodness of fit of the 7-TIS model[46] with the results of the experiments conducted, the mean absolute error (MAE) and the standard error of the mean (STDEM) were calculated as shown in eqs 12 and 13, respectively.[70,71]

$$\mathrm{MAE}_j = \sum_{i=1}^{n}\left|\frac{y_{\mathrm{exp}_{j,i}} - y_{\mathrm{TIS}_j}}{n}\right| \tag{12}$$

https://doi.org/10.1021/acs.iecr.4c02153
Ind. Eng. Chem. Res. 2024, 63, 18199−18211

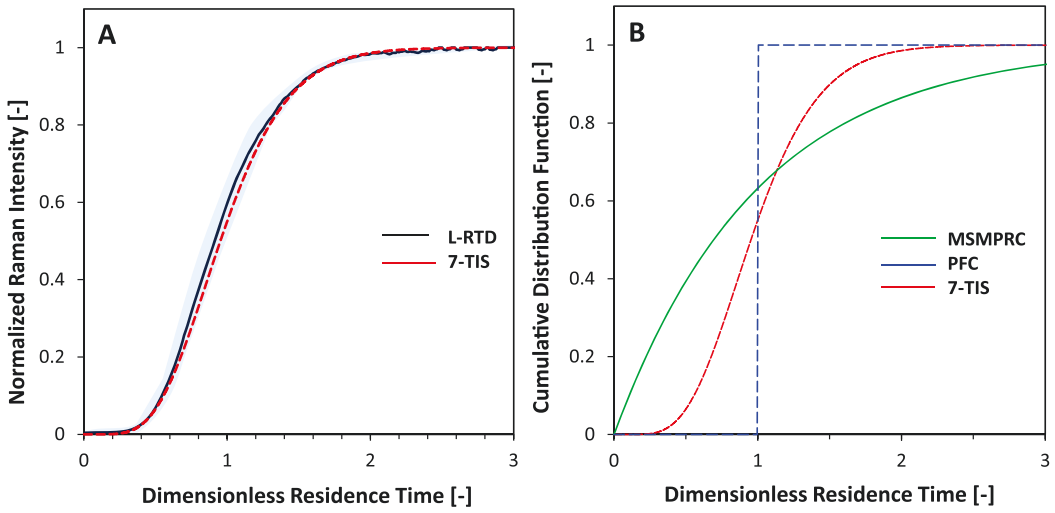

Figure 4. A) Normalized Raman intensity at 898 cm^{-1} representing the experimental cumulative liquid residence time distribution (RTD) obtained in the tower crystallizer (TWC, black line) compared with the 7-tank in series (TIS) model (red dashed line). The black trendline represents the average of three (n = 3) measurements, and the light blue area represents the standard error of the mean (STDEM). B) Comparison of theoretical (ideal) RTDs of single-stage mixed suspension mixed product removal crystallizer (MSMPRC, green solid line), plug flow crystallizer (PFC, blue solid line), and 7-TIS model (red dashed line).

$$\mathrm{STDEM}_j = \frac{\sigma_{\mathrm{exp}_j}}{\sqrt{n}} \tag{13}$$

Here, $y_{\mathrm{exp}_{i,j}}$ is the jth data point of the ith experiment, and y_{TIS_j} is the jth data point of 7-TIS model. The value n represents the total number of replicated experiments and $\sigma_{\mathrm{exp},j}$ is the standard deviation of an individual experiment at a given RTD data point. The STDEM_j represents the standard error of the mean between n experiments at the jth time point of the RTD.

3.1. Caveats in Data Analysis. It is important to emphasize some caveats in the mathematical data analysis detailed above. First, in a typical RTD experiment, detailed normalization is conducted using the total tracer material injected at the inlet, and then, the fraction of tracer material collected was calculated at the outlet. Important for S-RTD experiments, the total counts of tracer particles varied among the different test series conducted to evaluate the impact of particle size and slurry density. Moreover, the normalization method assumes based on conventional wisdom that all the tracer material will be recovered at the outlet, eventually, resulting in a final value for $F(t)$ = 1. At this point, though true for L-RTD (detailed below), it must be emphasized that for certain S-RTD experiments a fraction of the solid tracer was not fully recovered as shown in Figure S7, emphasizing a solids-dependent deviation from the ideality of the S-RTD in the TWC (further discussed below).

Second, it is important to emphasize that the mathematical characterization for S-RTD assumes that the particle size distribution remains constant throughout the experiment with no particle breakage and no classification (size-dependent transport).[46,53,69] The former would be evidenced by a size reduction of the solid tracers from before to after the experiments. The latter would be proven by a time-varying CSD in the CT and a deviation from the 7-TIS model. The particle size dependency of the results, underscoring the validity of the S-RTD analysis, is discussed in detail in Section 4.3.3.

Finally, it needs to be mentioned that the number of chord lengths measured using the Blaze probe is proportional to the size of the particles monitored.[61] However, evaluating in detail the complex correlation between the particle counts, particle size, and particle concentration was beyond the scope of the present work.

4. RESULTS AND DISCUSSION

4.1. Rationale for Stirring Rate. In the current work, the stirring rate of 2000 rpm was selected based on preliminary experiments with inert solids, visually observing sufficient mixing through the glass inspection windows of the TWC prototype (Figure 2A). Without claiming to be optimized, it was concluded that stirring rates <2000 rpm led to settling phenomena in the tanks. Some might argue that the stirring rate of 2000 rpm in each of the 11.4 mL tanks is unconventionally high for crystallization processes because typical stirring rates reported in lab-scale crystallizers (100–200 mL) range between 100 and 500 rpm.[47,72−76] However, the relatively small TWC impeller diameter (11 mm) at 2000 rpm results in the same 1.15 m/s tip speed[53] as calculated for a 38 mm impeller diameter[77,78] at 500 rpm in a lab-scale crystallizer (Figure S5). Thus, the TWC scales down with a similar impeller tip speed.[53,79]

Moreover, supporting control experiments prove the absence of the particle breakage of glycine particles (<800 μm) at stirring rates of 2000 and 2500 rpm, respectively (Figure S9). These experiments were conducted in an iterated version of the TWC reported in this article, allowing for in situ particle size measurements inside the TWC tanks using the Blaze probe (Figure S9).

Further considerations of the impact of the stirring rate on the TWC performance are beyond the scope of this article. However, as a vital aspect of the TWC prototype characterization, a separate article is being prepared focusing on the mixing optimization at lower stirring rates.

4.2. L-RTD Characterization. The characterization of L-RTD was conducted by tracking the concentration of glycine (tracer) in water via Raman spectroscopy. Glycine was selected

https://doi.org/10.1021/acs.iecr.4c02153
Ind. Eng. Chem. Res. 2024, 63, 18199−18211

given its extensive data reported in the literature.[56,59,80,81] Figure 4A depicts the average L-RTD of the pulse input experiments. The relatively narrow light blue area visually demonstrates the reproducibility of the L-RTD experiments measured in triplicate (STDEM ≤ 0.02).

In addition, it can be seen that the averaged L-RTD approaches well the theoretical TIS model for seven tanks well, also quantified by the small MAE = 0.03, thus ≤3% deviation. These results suggest close to ideal transport of the liquid (homogeneous) phase in the TWC. Thus, neither bypassing (RTD curve with an initial jump and long tail compared to the 7-TIS model) nor dead volume issues (the RTD curve shifted to the left of the 7-TIS model) were observed.[43,46] Figure S6 illustrates a schematic representation of these nonidealities. Since the 7-TIS model describes the TWC very well (Figure 4A), it can be concluded that the TWC (total volume, 80 mL) achieves a narrower L-RTD compared to a single-stage MSMPRC (typical settings, ≥100 mL volume)[47,72−76] while approaching a plug flow crystallizer (Figure 4B).[34,46] One might argue that mean RTs other than 15 min used in this study need to be investigated. However, experimental and theoretical work of single- and two-stage MSMPRCs have proved that both the flow rate and mean RT have negligible effects on the L-RTD performance.[47,72,82] Thus, extrapolated to the TWC, it was decided that further studies with varying mean RTs were not necessary.

4.3. S-RTD Characterization. *4.3.1. Rationale for S-RTD Measurement Approach.* Though studies have been reported in the literature employing the pulse input method for experimental S-RTD measurements using either dry solids or suspensions,[48−50] this approach was deemed unfeasible in this study because of the unique features of the TWC. Specifically, the TWC does not have a free surface, except in the last tank (Figure 1C), allowing for the addition of dry powder or large volumes of suspensions to achieve the relatively high slurry densities of 140−228 mg/mL studied in this work. Second, the relatively small orifices of the feed ports (≤1.5 mm, Figure 1A) are susceptible to clogging for these denser slurries with particle sizes <600 μm employed. On this account, it was decided to load the solids directly into the bottom tank of the disassembled TWC before starting the S-RTD experiments, as detailed in Section 2.3.2. Consequently, for the S-RTD experiments, the solid tracer was not instantaneously injected into a fully developed continuous flow field as defined for the pulse input method.[46,69] In contrast, the L-RTD assessment followed a more conventional tracer injection method. The rationale for the reported S-RTD measurement approach is based on the assumption that in stirred tanks, a homogeneous suspension is achieved within a few seconds (typically 5−30 s) upon the start of stirring.[83] This lag time of ≤30 s was deemed negligible (<2%) in the measurements for S-RTD lasting about ∼2RT, thus, ∼30 min to reach the maximum (Figure 5). Thus, the presence of solids at the start of the S-RTD experiments can be assumed as an instantaneous suspension pulse.[46] The proof of this assumption is discussed in the next section.

4.3.2. Effectiveness of Solid Transfer. Isokinetic suspension withdrawal is achieved in continuous crystallizers, when the removal rates of crystals in slurries (heterogeneous phase) and liquid (homogeneous phase) are identical.[27] To test whether isokinetic solid transfer occurs in the TWC, the first set of S-RTD experiments were focused on varying the slurry (suspension) density at a constant tracer particle size of <100 μm, as shown in Figure 5.

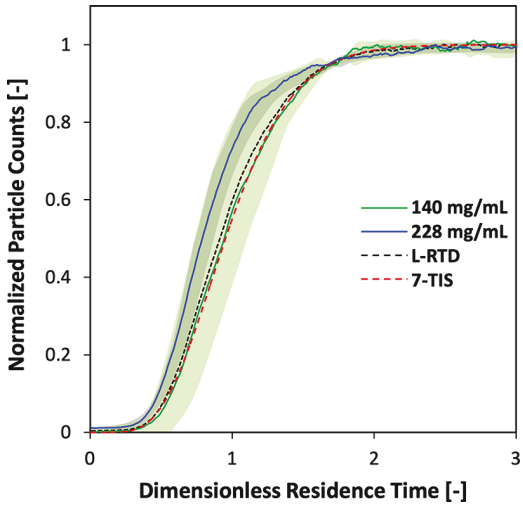

Figure 5. Impact of slurry density (SD) at 140 mg/mL (green solid line) and 228 mg/mL (blue solid line) on the cumulative solid residence time distribution (S-RTD) in the tower crystallizer (TWC) for particles <100 μm compared to L-RTD (black dashed line) and the 7-tank in series (TIS) model (red dashed line). The solid trendlines represent the average S-RTDs, and the shaded areas depict the standard error of the mean (STDEM) for SD = 140 mg/mL (green, n = 3) and 228 mg/mL (blue, n = 2).

The particle size of <100 μm was chosen because it represents a desired benchmark crystal size range for numerous pharmaceutical crystallization processes reported in the literature.[36,41,42,84−88] Similarly, the two slurry densities 140 and 228 mg/mL studied in this work are within the range commonly targeted for industrial crystallization processes.[5] From Figure 5, both slurry densities prove high reproducibility of the S-RTD curves with averaged STDEM values ≤5%. Figure 5 also reveals that increasing the slurry density does not significantly alter the S-RTD because the narrow STDEM area for 228 mg/mL is within the STDEM area for 140 mg/mL. One might argue that the slight shift of the S-RTD for 228 mg/mL slurry density to the left of the ideal 7-TIS model is an indication of nonideality (dead volume, Figure S6), which could be caused by larger particles keeping the nonreturn valves open (Figure 1B), allowing smaller particles to flow through the TWC faster. However, further studies are needed to exclude that the shift for $S\text{-}RTD_{228}$ (only measured in duplicate) is simply within the error of the S-RTD experiments, considering that the STDEM range for 140 mg/mL exceeds the one for 228 mg/mL while matching the 7-TIS model very well (Figure 5). This assessment is supported by the fact that upon disassembling the TWC (Figure 1B) at the end of the $S\text{-}RTD_{228}$ experiments, no particles were visually observed inside the tanks. Though the beginning of nonideality for the slurry density of 228 mg/mL cannot be fully excluded, with the data presented it is likely to be concluded that the S-RTD curves for the studied particle size of ≤100 μm and slurry densities of 140 and 228 mg/mL demonstrate good agreement with those of the L-RTD and 7-TIS model ($MAE_{140} \leq 4\%$ and $MAE_{228} \leq 10\%$). This conclusion confirms the capabilities of the novel TWC to ensure effective solid transfer that enables isokinetic suspension withdrawal during crystallization processes for slurry densities close to 228 mg/mL.

4.3.3. Range of Particle Size. To further map out the TWC prototype, the second set of S-RTD experiments focused on

https://doi.org/10.1021/acs.iecr.4c02153
Ind. Eng. Chem. Res. 2024, 63, 18199−18211

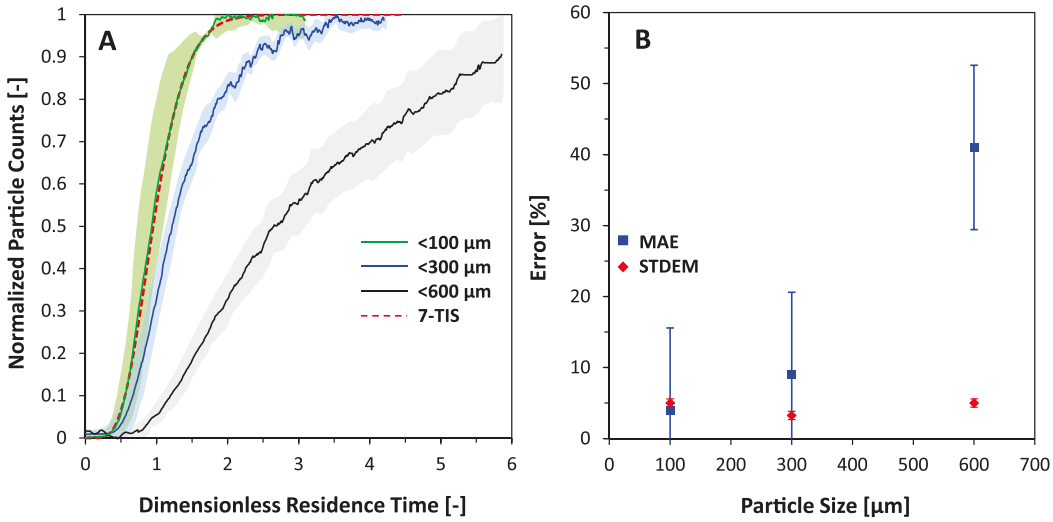

Figure 6. A) Experimental cumulative solid residence time distributions (S-RTD) in the tower crystallizer (TWC) for particle sizes <100 μm (green solid line), < 300 μm (blue solid line), and <600 μm (black solid line) compared to the 7-tank in series (TIS) model (red dashed line). The solid trendlines represent the average of three (n = 3) measurements, and the shaded areas represent the standard error of the mean (STDEM). B) STDEM and mean absolute error (MAE) for the S-RTD experiments with different particle sizes. If error bars are not visible, they are hidden behind the data points.

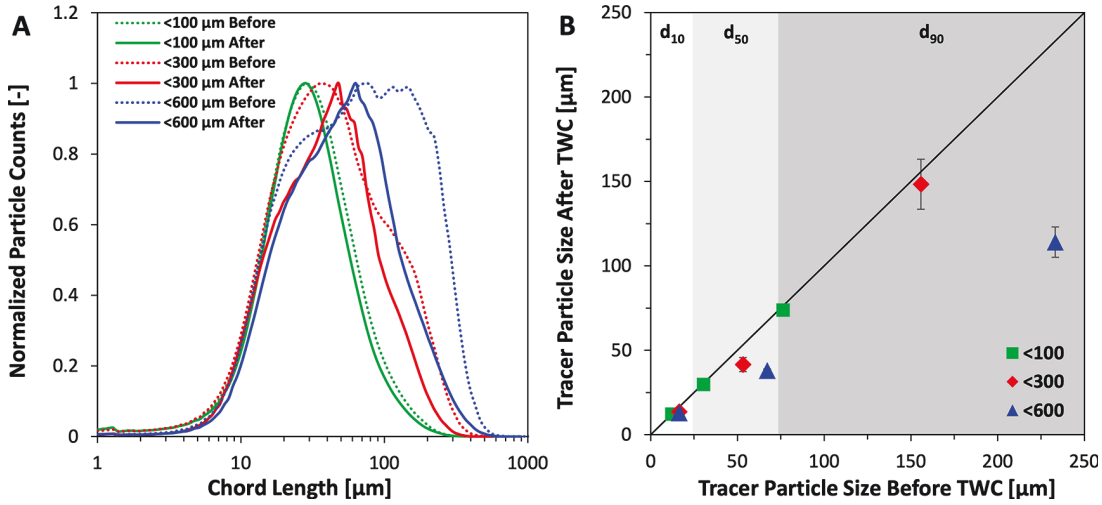

Figure 7. A) Comparison of image-derived chord length distribution (ID-CLD) of glycine crystals (tracer) before (broken lines) and after (solid lines) solid residence time distribution (S-RTD) experiments. B) Comparison of the tracer particle size (percentiles) d_{10}, d_{50} (light gray), and d_{90} (dark gray) of the ID-CLDs depicted in (A) before and after S-RTD. If error bars are not visible, they are hidden behind the data points.

testing whether the TWC can handle particle sizes of >100 μm at a constant slurry density of 140 mg/mL. Figure 6 summarizes the experimental S-RTDs determined for three different particle sizes (<100, <300, <600 μm).

Though all experiments show high reproducibility with STDEM $\leq$ 5%, the cumulative S-RTD curves reveal a deviation from the theoretical 7-TIS model with increasing particle size (Figure 6A). Specifically, while the S-RTD for <100 μm particles aligns very well with the 7- TIS model ($MAE_{100\ \mu m} \leq 4\%$), the S-RTDs for <300 and <600 μm demonstrate increasing deviations ($MAE_{300\ \mu m} \leq 9\%$ and $MAE_{600\ \mu m} \leq 41\%$), as illustrated in Figure 6B. These results indicate that >100 μm particles do not follow an isokinetic transport through the TWC. To further understand the particle size-dependent S-RTD results, Figure 7A compares the ID-CLDs of the tracers before and after the S-RTD experiments.

While the tracer with <100 μm particles maintained a constant ID-CLD (Figure 7A), the ID-CLDs for larger particles shifted to smaller values, indicating a size classification[5] of the particles within the TWC. The size reduction is especially obvious for the <600 μm tracer.[89] This assessment is supported by the comparison of the ID-CLD derived percentiles d_{10}, d_{50}, and d_{90} (Figure 7B). Generally, the closer the data points for the three percentiles (different shaded areas) are visually plotted to the 45° black solid line, the less classification occurred. Data points above the black solid line would indicate growth or agglomeration, which did not occur due to the S-RTD experiments being conducted in antisolvent at constant temperature. The percentiles for the <100 μm tracer match very well the 45° line, while the tracer with <600 μm particles demonstrate significant size reduction. Interestingly, the percentiles for the <300 μm tracer are relatively close to the 45° line and for the d_{90} even within the

https://doi.org/10.1021/acs.iecr.4c02153
Ind. Eng. Chem. Res. 2024, 63, 18199−18211

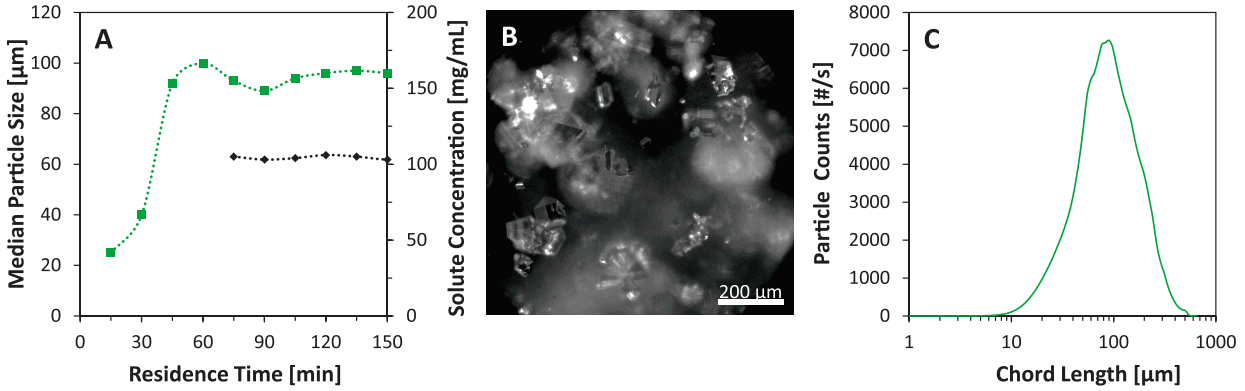

Figure 8. Experimental results of the continuous antisolvent crystallization of glycine in a tower crystallizer (TWC). A) Evolution of the length-weighted (LW) median chord length (green, left *y*-axis) and solute concentration at the TWC exit (black, right *y*-axis) from the start of the continuous experiment (the solute concentration was monitored once the solid signals stabilized, after ∼5 residence times (RTs). B) Representative in-line microscopy image of crystallized glycine. C) Image-derived chord length distribution (LW) at steady state (after 10 RT, thus, 150 min).

error bars of the measurements. This result hints that the particle size limit, the TWC prototype can handle in its current configuration without size classification, is likely closer to 300 μm. This conclusion is supported by the fact that the S-RTD of the <300 μm tracer in comparison to the 7-TIS model deviates ≤9% (Figure 6B, MAE). Moreover, this assessment hints that >100 μm particles but <300 μm particles are transported in the TWC not in accordance with the liquid phase, and thus the 7-TIS model (Figure 6A). Micrographs of the disassembled TWC after the S-RTD experiments proved the presence of crystals inside the TWC (Figure S7). Interestingly, the crystals are not trapped in the first tank but are evenly distributed throughout the tanks of the TWC, indicating that the transport of >100 μm particles are not entrapped but rather slowed down in the TWC compared to the liquid phase (L-RTD). Similar differences between L-RTD and S-RTD have been reported in studies focused on both MSMPRs[5,90] and tubular-type crystallizers[50,91] without providing conclusive discussion.

To further understand the deviation between the L-RTD and S-RTD in the TWC more research is needed, which goes beyond the scope of this article. Specifically, future studies should examine the TWC's ability to handle different particle shapes (e.g., needlelike, plate-like)[42] and solid-to-liquid density ratios. Glycine crystals used in this study are prismatic[55] with a density ratio (glycine/ethanol) of 2.[92] In addition, the correlation between the suspension density and particle size on the flow behavior needs to be understood. Based on the data presented in this article, it is hypothesized that decreasing the slurry density <140 mg/mL for the tracer with particles <300 μm will decrease the deviation from the 7-TIS model (MAE). Specifically, it is assumed that lower slurry densities reduce the disturbance in the particle movement, particularly when transported through the relatively narrow intertank clearances (ID = 1 mm) and openings of the nonreturn valves in the push mode of the TWC (Figure 1).

4.4. Proof-of-Concept Continuous Antisolvent Crystallization. To further test the TWC, a proof-of-concept antisolvent continuous crystallization was performed targeting a similar crystal size (≤100 μm), as favorably assessed in the S-RTD study above. The crystallization process with a mean RT of 15 min, a feed concentration of 200 mg/mL for the fast-growing model compound glycine[47] in water, and an antisolvent (ethanol) to solvent volume ratio of 0.15 was designed to limit the supersaturation ($S = \frac{c}{c^*}$)[1] available for crystal growth to S = 1.14, while allowing nucleation without seeding.[64] Figure 8 summarizes the experimental results.

Figure 8A shows that the median particle size (chord length) and the mother liquor concentration yielded relatively constant values after ∼5 RT, indicating that the continuous crystallization process approached a steady state. Thereafter, the TWC operated for a total of 10 RT without fouling and clogging. No particle entrapment, clogging, or fouling was visually observed upon opening the TWC at the end of the crystallization experiment. Once steady state was reached, the average median particle size for ≥5 RT was 94.0 ± 2.5 μm. In addition, based on the mother liquor concentration and reported solubility data[65] (Section S8), a slurry density of 20 mg/mL was maintained at steady state. More importantly, the consistent signals in Figure 8A prove the capability of the novel diaphragm-driven slurry transfer of the TWC to deliver consistent and accurate pulsations of the crystal slurries without causing fluctuations in the quality metrics for this first proof-of-concept continuous crystallization in the TWC.

The generated crystals possess sharp edges, proving the absence of significant crystal breakage and abrasion in the TWC operated at a stirring rate of 2000 rpm (Figure 8B). Control experiments summarized in Section S9 further substantiate this assessment. The prismatic morphology of the obtained glycine crystals provides a hint that the stable α form of glycine was crystallized.[80] No powder X-ray characterization was conducted in this study, because polymorph control was not the focus.

Finally, the ID-CLD of the crystallized glycine at a steady state demonstrates a unimodal distribution (Figure 8C). This result is very likely facilitated through the unique near plug flow characteristics in the TWC, as demonstrated in the L-RTD and S-RTD measurements (Figures 4 and 5). Though beyond the scope of this proof-of-concept article, future work will focus on the comparison with other crystallizer types to clearly explore the advantages and limits of the TWC. Such a comparison is a vital aspect for the TWC evaluation and contributes to the unmet need for crystallization comparison studies for the same compound in different types of crystallizers.[3]

Finally, one might argue that >100 μm particles were produced in the crystallization experiment (Figure 8B), which

https://doi.org/10.1021/acs.iecr.4c02153
Ind. Eng. Chem. Res. 2024, 63, 18199−18211

might seem in contradiction with the S-RTD conclusions (Figure 7). However, one must bear in mind that in the S-RTD experiments, first, the tracers were loaded in the first tank of the TWC, resulting in slurry densities of 140 and 228 mg/mL, respectively. Thus, while the particles in the S-RTD experiments were transported through all seven tanks of the TWC, during the crystallization experiment, the glycine crystals likely grew throughout the TWC, reaching the largest size in the latter tanks. Second, the slurry density during the crystallization experiment reached 20 mg/mL at the end of the crystallizer, thus significantly less than that in the S-RTD experiments, where the slurry density was higher throughout the TWC. The latter supports the hypothesis that reducing the slurry density will likely improve the solids transport of larger particles through the TWC. Third, it is important to recall that the S-RTD experiments show that large particles (>300 μm) are transported slower through the TWC. However, they are still recovered eventually. Therefore, the ID-CLD observed in Figure 8C showing larger particle sizes is consistent with the results from the S-RTD experiments. However, the maximum size the TWC can handle was not conclusively determined in this proof-of-concept study and requires further investigations.

5. CONCLUSION

The presented work demonstrated the development of a novel continuous crystallizer consisting of a series of seven miniaturized MSMPRCs (80 mL total volume), developed by Zaiput Flow Technologies, featuring a proprietary diaphragm-driven slurry transfer system. The RTD of the liquid phase followed the 7-TIS model, indicating ideal mixing behavior. <100 μm particles, which are a common benchmark in the crystallization of APIs, were equally well transported (no size classification, S-RTD in agreement with L-RTD) at a suspension density of 140 mg/mL. At a higher slurry density of 228 mg/mL, the beginning of nonideal flow behavior inside the TWC might have been observed (no size classification, but deviation from L-RTD). However, further studies have been suggested to be conclusive. Isokinetic withdrawal is of vital importance for the characterization, prediction, and control of continuous crystallization processes. Here, S-RTD experiments with tracer particles in the 300 and 600 μm range were subjected to size classification, signaling that further optimization of the mixing conditions and vertical slurry transport is required. A proof-of-concept unseeded crystallization experiment produced nonaggregated glycine crystals with a unimodal CSD. Future efforts will be taken to evaluate the impact of multiple antisolvent injection points on the crystal quality by providing more control over the desupersaturation profiles throughout the TWC. Finally, hardware development work will focus on the optimization of the hydrodynamics inside the crystallizer in terms of mixing efficiency and design modifications to enable temperature-driven crystallization inside the TWC.

■ ASSOCIATED CONTENT

Supporting Information

The Supporting Information is available free of charge at https://pubs.acs.org/doi/10.1021/acs.iecr.4c02153.

Raman spectra of aqueous glycine solutions; raw data of residence time distribution (RTD) measurements; rationale on the use of a flow-cell for RTD measurements; impeller tip speed evaluation; characterization of nonideal RTD; micrographs of disassembled crystallizer after S-RTD experiments; percentiles of particle size distributions; glycine solubility in water/ethanol solutions; and particle breakage test (PDF)

■ AUTHOR INFORMATION

Corresponding Author

Torsten Stelzer − *Department of Chemical Engineering, Massachusetts Institute of Technology, Cambridge, Massachusetts 02139, United States; Department of Pharmaceutical Sciences, University of Puerto Rico, San Juan, Puerto Rico 00936, United States; Crystallization Design Institute, Molecular Sciences Research Center, University of Puerto Rico, San Juan, Puerto Rico 00926, United States;* orcid.org/0000-0003-3881-0183; Email: torsten.stelzer@upr.edu

Authors

Giovanni Aprile − *Department of Chemical Engineering, Massachusetts Institute of Technology, Cambridge, Massachusetts 02139, United States; Department of Chemical and Biochemical Engineering, Technical University of Denmark DTU, Kongens Lyngby 2800, Denmark; H. Lundbeck A/S, Valby 2500, Denmark;* orcid.org/0000-0001-6549-3107

Ajinkya V. Pandit − *Department of Chemical Engineering, Massachusetts Institute of Technology, Cambridge, Massachusetts 02139, United States*

Jody Albertazzi − *Department of Chemistry, Materials and Chemical Engineering "G. Natta,", Politecnico di Milano, Milan 20133, Italy*

Thomas Vetter − *H. Lundbeck A/S, Valby 2500, Denmark*

Robert Viano − *Zaiput Flow Technologies, Waltham, Massachusetts 02451, United States*

Lorenzo Milani − *Zaiput Flow Technologies, Waltham, Massachusetts 02451, United States*

Andrea Adamo − *Zaiput Flow Technologies, Waltham, Massachusetts 02451, United States;* orcid.org/0000-0002-7406-706X

Allan S. Myerson − *Department of Chemical Engineering, Massachusetts Institute of Technology, Cambridge, Massachusetts 02139, United States;* orcid.org/0000-0002-7468-8093

Complete contact information is available at: https://pubs.acs.org/10.1021/acs.iecr.4c02153

Funding

This study was supported by the National Science Foundation (NSF) under the Advanced Manufacturing Program (CMMI-2242255) and DeNOVX (subcontract NIH SBIR grant no. 2R44TR001380−02A). Giovanni Aprile was supported by the Technical University of Denmark and Lundbeck A/S.

Notes

The authors declare the following competing financial interest(s): The authors declare no competing financial interest, except Andrea Adamo, who has some stock ownership of Zaiput Flow Technologies.

■ REFERENCES

(1) O'Mahony, M.; Ferguson, S.; Stelzer, T.; Myerson, A. Separation and Purification in the Continuous Synthesis of Fine Chemicals and Pharmaceuticals. In *Science of Synthesis: Flow Chemistry in Organic Synthesis*; Georg Thieme Verlag KG, 2018; pp. 51102.

(2) Stelzer, T.; Lakerveld, R.; Myerson, A. S. Process Intensification in Continuous Crystallization. In *The Handbook of Continuous Crystallization*; The Royal Society of Chemistry, 2020; pp. 266320.
(3) Wood, B.; Girard, K. P.; Polster, C. S.; Croker, D. M. Progress to Date in the Design and Operation of Continuous Crystallization Processes for Pharmaceutical Applications. *Org. Process Res. Dev.* **2019**, *23* (2), 122−144.
(4) Cote, A.; Erdemir, D.; Girard, K. P.; Green, D. A.; Lovette, M. A.; Sirota, E.; Nere, N. K. Perspectives on the Current State, Challenges, and Opportunities in Pharmaceutical Crystallization Process Development. *Cryst. Growth Des.* **2020**, *20*, 7568−7581.
(5) Myerson, A. S.; Erdemir, D.; Lee, A. Y. *Handbook of Industrial Crystallization*, 3rd ed.; Cambridge University Press: Cambridge, 2019.
(6) Chen, J.; Sarma, B.; Evans, J. M. B.; Myerson, A. S. Pharmaceutical Crystallization. *Cryst. Growth Des.* **2011**, *11* (4), 887−895.
(7) Hessel, V. Novel Process Windows − Gate to Maximizing Process Intensification via Flow Chemistry. *Chem. Eng. Technol.* **2009**, *32* (11), 1655−1681.
(8) Hartman, R. L.; McMullen, J. P.; Jensen, K. F. Deciding Whether To Go with the Flow: Evaluating the Merits of Flow Reactors for Synthesis. *Angew. Chem., Int. Ed.* **2011**, *50* (33), 7502−7519.
(9) Lakerveld, R.; Heider, P. L.; Jensen, K. D.; Braatz, R. D.; Jensen, K. F.; Myerson, A. S.; Trout, B. L. End to End Continuous Manufacturing: Integration of Unit Operations. *Continuous Manufacturing of Pharmaceuticals* **2017**, 447−483.
(10) May, S. A. Flow Chemistry, Continuous Processing, and Continuous Manufacturing: A Pharmaceutical Perspective. *J. Flow Chem.* **2017**, *7* (3), 137−145.
(11) Plutschack, M. B.; Pieber, B.; Gilmore, K.; Seeberger, P. H. The Hitchhiker's Guide to Flow Chemistry. *Chem. Rev.* **2017**, *117* (18), 11796−11893.
(12) Cole, K. P.; Groh, J. M.; Johnson, M. D.; Burcham, C. L.; Campbell, B. M.; Diseroad, W. D.; Heller, M. R.; Howell, J. R.; Kallman, N. J.; Koenig, T. M.; May, S. A.; Miller, R. D.; Mitchell, D.; Myers, D. P.; Myers, S. S.; Phillips, J. L.; Polster, C. S.; White, T. D.; Cashman, J.; Hurley, D.; Moylan, R.; Sheehan, P.; Spencer, R. D.; Desmond, K.; Desmond, P.; Gowran, O. Kilogram-Scale Prexasertib Monolactate Monohydrate Synthesis under Continuous-Flow CGMP Conditions. *Science* **2017**, *356*, 1144−1150.
(13) Malet-Sanz, L.; Susanne, F. Continuous Flow Synthesis. A Pharma Perspective. *J. Med. Chem.* **2012**, *55* (9), 4062−4098.
(14) Hessel, V.; Kralisch, D.; Kockmann, N.; Noël, T.; Wang, Q. Novel Process Windows for Enabling, Accelerating, and Uplifting Flow Chemistry. *ChemSuschem* **2013**, *6* (5), 746−789.
(15) Yoshida, J.-i.; Takahashi, Y.; Nagaki, A. Flash Chemistry: Flow Chemistry That Cannot Be Done in Batch. *Chem. Commun.* **2013**, *49* (85), 9896−9904.
(16) Baumann, M.; Baxendale, I. R. The Synthesis of Active Pharmaceutical Ingredients (APIs) Using Continuous Flow Chemistry. *Beilstein J. Org. Chem.* **2015**, *11*, 1194−1219.
(17) Gutmann, B.; Cantillo, D.; Kappe, C. O. Continuous-Flow Technology—A Tool for the Safe Manufacturing of Active Pharmaceutical Ingredients. *Angew. Chem., Int. Ed.* **2015**, *54* (23), 6688−6728.
(18) Porta, R.; Benaglia, M.; Puglisi, A. Flow Chemistry: Recent Developments in the Synthesis of Pharmaceutical Products. *Org. Process Res. Dev.* **2016**, *20* (1), 2−25.
(19) Fitzpatrick, D. E.; Battilocchio, C.; Ley, S. V. Enabling Technologies for the Future of Chemical Synthesis. *ACS Cent. Sci.* **2016**, *2*, 131−138.
(20) Gutmann, B.; Kappe, C. O. Forbidden Chemistries — Paths to a Sustainable Future Engaging Continuous Processing. *J. Flow Chem.* **2017**, *7* (3), 65−71.
(21) Ierapetritou, M.; Muzzio, F.; Reklaitis, G. Perspectives on the Continuous Manufacturing of Powder-Based Pharmaceutical Processes. *AICHE J.* **2016**, *62* (6), 1846−1862.
(22) Ierapetritou, M. G.; Ramachandran, R. *Process Simulation and Data Modeling in Solid Oral Drug Development and Manufacture*; Humana Press, 2016.
(23) Vanhoorne, V.; Vervaet, C. Recent Progress in Continuous Manufacturing of Oral Solid Dosage Forms. *Int. J. Pharm.* **2020**, *579*, 119194.
(24) Moghtadernejad, S.; Escotet-Espinoza, M. S.; Oka, S.; Singh, R.; Liu, Z.; Román-Ospino, A. D.; Li, T.; Razavi, S.; Panikar, S.; Scicolone, J.; Callegari, G.; Hausner, D.; Muzzio, F. A Training on: Continuous Manufacturing (Direct Compaction) of Solid Dose Pharmaceutical Products. *J. Pharm. Innovation* **2018**, *13*, 155−187.
(25) Cole, K. P.; Reizman, B. J.; Hess, M.; Groh, J. M.; Laurila, M. E.; Cope, R. F.; Campbell, B. M.; Forst, M. B.; Burt, J. L.; Maloney, T. D.; Johnson, M. D.; Mitchell, D.; Polster, C. S.; Mitra, A. W.; Boukerche, M.; Conder, E. W.; Braden, T. M.; Miller, R. D.; Heller, M. R.; Phillips, J. L.; Howell, J. R. Small-Volume Continuous Manufacturing of Merestinib. Part 1. Process Development and Demonstration. *Org. Process Res. Dev.* **2019**, *23* (5), 858−869.
(26) Reizman, B. J.; Cole, K. P.; Hess, M.; Burt, J. L.; Maloney, T. D.; Johnson, M. D.; Laurila, M. E.; Cope, R. F.; Luciani, C. V.; Buser, J. Y.; Campbell, B. M.; Forst, M. B.; Mitchell, D.; Braden, T. M.; Lippelt, C. K.; Boukerche, M.; Starkey, D. R.; Miller, R. D.; Chen, J.; Sun, B.; Kwok, M.; Zhang, X.; Tadayon, S.; Huang, P. Small-Volume Continuous Manufacturing of Merestinib. Part 2. Technology Transfer and CGMP Manufacturing. *Org. Process Res. Dev.* **2019**, *23* (5), 870−881.
(27) Randolph, A. D.; Larson, M. A. *Theory of Particulate Processes*, 2nd ed.; Academic Press, Inc., 1988.
(28) Alvarez, A. J.; Myerson, A. S. Continuous Plug Flow Crystallization of Pharmaceutical Compounds. *Cryst. Growth Des.* **2010**, *10* (5), 2219−2228.
(29) Majumder, A.; Nagy, Z. K. Dynamic Modeling of Encrust Formation and Mitigation Strategy in a Continuous Plug Flow Crystallizer. *Cryst. Growth Des.* **2015**, *15* (3), 1129−1140.
(30) Jiang, M.; Zhu, Z.; Jimenez, E.; Papageorgiou, C. D.; Waetzig, J.; Hardy, A.; Langston, M.; Braatz, R. D. Continuous-Flow Tubular Crystallization in Slugs Spontaneously Induced by Hydrodynamics. *Cryst. Growth Des.* **2014**, *14* (2), 851−860.
(31) Jiang, M.; Braatz, R. D. Designs of Continuous-Flow Pharmaceutical Crystallizers: Developments and Practice. *CrystEngcomm* **2019**, *21* (23), 3534−3551.
(32) McGlone, T.; Briggs, N. E. B. B.; Clark, C. A.; Brown, C. J.; Sefcik, J.; Florence, A. J. Oscillatory Flow Reactors (OFRs) for Continuous Manufacturing and Crystallization. *Org. Process Res. Dev.* **2015**, *19* (9), 1186−1202.
(33) Peña, R.; Oliva, J. A.; Burcham, C. L.; Jarmer, D. J.; Nagy, Z. K. Process Intensification through Continuous Spherical Crystallization Using an Oscillatory Flow Baffled Crystallizer. *Cryst. Growth Des.* **2017**, *17* (9), 4776−4784.
(34) Vetter, T.; Burcham, C. L.; Doherty, M. F. Regions of Attainable Particle Sizes in Continuous and Batch Crystallization Processes. *Chem. Eng. Sci.* **2014**, *106*, 167−180.
(35) Hou, G.; Power, G.; Barrett, M.; Glennon, B.; Morris, G.; Zhao, Y. Development and Characterization of a Single Stage Mixed-Suspension, Mixed-Product-Removal Crystallization Process with a Novel Transfer Unit. *Cryst. Growth Des.* **2014**, *14* (4), 1782−1793.
(36) Quon, J. L.; Zhang, H.; Alvarez, A.; Evans, J.; Myerson, A. S.; Trout, B. L. Continuous Crystallization of Aliskiren Hemifumarate. *Cryst. Growth Des.* **2012**, *12* (6), 3036−3044.
(37) Ferguson, S.; Morris, G.; Hao, H.; Barrett, M.; Glennon, B. Characterization of the Anti-Solvent Batch, Plug Flow and MSMPR Crystallization of Benzoic Acid. *Chem. Eng. Sci.* **2013**, *104*, 44−54.
(38) Polster, C. S.; Cole, K. P.; Burcham, C. L.; Campbell, B. M.; Frederick, A. L.; Hansen, M. M.; Harding, M.; Heller, M. R.; Miller, M. T.; Phillips, J. L.; Pollock, P. M.; Zaborenko, N. Pilot-Scale Continuous Production of LY2886721: Amide Formation and Reactive Crystallization. *Org. Process Res. Dev.* **2014**, *18* (11), 1295−1309.

https://doi.org/10.1021/acs.iecr.4c02153
Ind. Eng. Chem. Res. 2024, 63, 18199−18211

(39) Zhang, H.; Quon, J.; Alvarez, A. J.; Evans, J.; Myerson, A. S.; Trout, B. Development of Continuous Anti-Solvent/Cooling Crystallization Process Using Cascaded Mixed Suspension, Mixed Product Removal Crystallizers. *Org. Process Res. Dev.* **2012**, *16* (5), 915−924.
(40) Ferguson, S.; Ortner, F.; Quon, J.; Peeva, L.; Livingston, A.; Trout, B. L.; Myerson, A. S. Use of Continuous MSMPR Crystallization with Integrated Nanofiltration Membrane Recycle for Enhanced Yield and Purity in API Crystallization. *Cryst. Growth Des.* **2014**, *14* (2), 617−627.
(41) Li, J.; Lai, T.-T. C.; Trout, B. L.; Myerson, A. S. Continuous Crystallization of Cyclosporine: Effect of Operating Conditions on Yield and Purity. *Cryst. Growth Des.* **2017**, *17*, 1000−1007.
(42) Cui, Y.; O'Mahony, M.; Jaramillo, J. J.; Stelzer, T.; Myerson, A. S. Custom-Built Miniature Continuous Crystallization System with Pressure-Driven Suspension Transfer. *Org. Process Res. Dev.* **2016**, *20* (7), 1276−1282.
(43) Tavare, N. S. Mixing in Continuous Crystallizers. *AICHE J.* **1986**, *32* (5), 705−732.
(44) Palma, M.; Giudici, R. Analysis of Axial Dispersion in an Oscillatory-Flow Continuous Reactor. *Chem. Eng. J.* **2003**, *94*, 189−198.
(45) Mo, Y.; Jensen, K. F. A Miniature CSTR Cascade for Continuous Flow of Reactions Containing Solids. *React. Chem. Eng.* **2016**, *1* (5), 501−507.
(46) Fogler, H. S. Distributions of Residence Times for Chemical Reactors. In *Elements of Chemical Reaction Engineering*; Prentice Hall, 2008; pp. 867944.
(47) Onyemelukwe, I. I.; Parsons, A. R.; Wheatcroft, H. P.; Robertson, A.; Nagy, Z. K.; Rielly, C. D. The Role of Residence Time Distribution in the Continuous Steady-State Mixed Suspension Mixed Product Removal Crystallization of Glycine. *Cryst. Growth Des.* **2019**, *19* (1), 66−80.
(48) Pomberger, A.; Mo, Y.; Nandiwale, K. Y.; Schultz, V. L.; Duvadie, R.; Robinson, R. I.; Altinoglu, E. I.; Jensen, K. F. A Continuous Stirred-Tank Reactor (CSTR) Cascade for Handling Solid-Containing Photochemical Reactions. *Org. Process Res. Dev.* **2019**, *23* (12), 2699−2706.
(49) Udepurkar, A. P.; Nandiwale, K. Y.; Jensen, K. F.; Kuhn, S. Heterogeneous Photochemical Reaction Enabled by an Ultrasonic Microreactor. *React. Chem. Eng.* **2023**, *8* (8), 1930−1936.
(50) Kacker, R.; Regensburg, S. I.; Kramer, H. J. M. Residence Time Distribution of Dispersed Liquid and Solid Phase in a Continuous Oscillatory Flow Baffled Crystallizer. *Chem. Eng. J.* **2017**, *317*, 413−423.
(51) Scargiali, F.; Grisafi, F.; Cermakova, J.; Machon, V.; Brucato, A. Particle Flow Modeling in Slurry-Fed Stirred Vessels. *Chem. Eng. Technol.* **2004**, *27* (3), 249−256.
(52) Scargiali, F.; Grisafi, F.; Cermakova, J.; Machon, V.; Brucato, A. Residence Time Distribution of Solid Particles in a Continuous, High-Aspect-Ratio Multiple-Impeller Stirred Vessel. *Chem. Eng. Sci.* **2004**, *59* (17), 3601−3618.
(53) Paul, E. L.; Atiemo-Obeng, V. A.; Kresta, S. M. *Handbook of Industrial Mixing*; John Wiley & Sons, Inc., 2003.
(54) Dickens, A. W.; Mackley, M. R.; Williams, H. R. Experimental Residence Time Distribution Measurements for Unsteady Flow in Baffled Tubes. *Chem. Eng. Sci.* **1989**, *44* (7), 1471−1479.
(55) Nii, S.; Takayanagi, S. Growth and Size Control in Anti-Solvent Crystallization of Glycine with High Frequency Ultrasound. *Ultrason. Sonochem.* **2014**, *21* (3), 1182−1186.
(56) Weiss, I. M.; Muth, C.; Drumm, R.; Kirchner, H. O. K. Thermal Decomposition of the Amino Acids Glycine, Cysteine, Aspartic Acid, Asparagine, Glutamic Acid, Glutamine, Arginine and Histidine. *BMC Biophys.* **2018**, *11* (2), 1−15.
(57) Bakar, M. R. A.; Nagy, Z. K.; Saleemi, A. N.; Rielly, C. D. The Impact of Direct Nucleation Control on Crystal Size Distribution in Pharmaceutical Crystallization Processes. *Cryst. Growth Des.* **2009**, *9* (3), 1378−1384.
(58) Devos, C.; Brozzi, E.; Van Gerven, T.; Kuhn, S. Characterization of a Modular Microfluidic Section for Seeded Nucleation in Multiphase Flow. *Org. Process Res. Dev.* **2023**, *27* (2), 311−321.
(59) Zhu, G.; Zhu, X.; Fan, Q.; Wan, X. Raman Spectra of Amino Acids and Their Aqueous Solutions. *Spectrochim. Acta, Part A* **2011**, *78* (3), 1187−1195.
(60) Liu, J.; Sun, J.; Huang, X.; Li, G. Goldindec: A Novel Algorithm for Raman Spectrum Baseline Correction. *Appl. Spectrosc.* **2015**, *69* (7), 834−842.
(61) Blaze Metrics, L. L. C. *Gen 1 through Gen 2.5 BlazeBasic, and BlazePlatform Manual Blaze UI and Office Software 148.03.10*. Quil Ceda Village, WA, USA, 2023.
(62) Howard, K. S.; Nagy, Z. K.; Saha, B.; Robertson, A. L.; Steele, G.; Martin, D. A Process Analytical Technology Based Investigation of the Polymorphic Transformations during the Antisolvent Crystallization of Sodium Benzoate from IPA/Water Mixture. *Cryst. Growth Des.* **2009**, *9* (9), 3964−3975.
(63) Beckmann, W. *Crystallization: Basic Concepts and Industrial Applications*; Wiley-VCH Verlag GmbH & Co. KGaA: Weinheim, Germany, 2013.
(64) Mou, M.; Jiang, M. Fast Continuous Non-Seeded Cooling Crystallization of Glycine in Slug Flow: Pure α-Form Crystals with Narrow Size Distribution. *J. Pharm. Innovation* **2020**, *15* (2), 281−294.
(65) Cao, Z.; Hu, Y.; Li, J.; Kai, Y.; Yang, W. Solubility of Glycine in Binary System of Ethanol+water Solvent Mixtures: Experimental Data and Thermodynamic Modeling. *Fluid Phase Equilib.* **2013**, *360*, 156−160.
(66) Myerson, A. S.; Krumme, M.; Nasr, M.; Thomas, H.; Braatz, R. D. Control Systems Engineering in Continuous Pharmaceutical Manufacturing May 20−21, 2014 Continuous Manufacturing Symposium. *J. Pharm. Sci.* **2015**, *104* (3), 832−839.
(67) Zauner, R.; Jones, A. G. On the Influence of Mixing on Crystal Precipitation Processes-Application of the Segregated Feed Model. *Chem. Eng. Sci.* **2002**, *57* (5), 821−831.
(68) Kacker, R.; Maaß, S.; Emmerich, J.; Kramer, H. Application of Inline Imaging for Monitoring Crystallization Process in a Continuous Oscillatory Baffled Crystallizer. *AICHE J.* **2018**, *64* (7), 2450−2461.
(69) Levenspiel, O. *Chemical Reaction Engineering*, 3rd ed.; John wiley & Sons, 1998.
(70) Jiang, M.; Papageorgiou, C. D.; Waetzig, J.; Hardy, A.; Langston, M.; Braatz, R. D. Indirect Ultrasonication in Continuous Slug-Flow Crystallization. *Cryst. Growth Des.* **2015**, *15* (5), 2486−2492.
(71) Öner, M.; Montes, F. C. C.; Ståhlberg, T.; Stocks, S. M.; Bajtner, J. E.; Sin, G. Comprehensive Evaluation of a Data Driven Control Strategy: Experimental Application to a Pharmaceutical Crystallization Process. *Chem. Eng. Res. Des.* **2020**, *163*, 248−261.
(72) Choi, B. S.; Wan, B.; Philyaw, S.; Dhanasekharan, K.; Ring, T. A. Residence Time Distributions in a Stirred Tank - Comparison of CFD Predictions with Experiment. *Ind. Eng. Chem. Res.* **2004**, *43*, 6548−6556.
(73) Lai, T. T. C.; Cornevin, J.; Ferguson, S.; Li, N.; Trout, B. L.; Myerson, A. S. Control of Polymorphism in Continuous Crystallization via Mixed Suspension Mixed Product Removal Systems Cascade Design. *Cryst. Growth Des.* **2015**, *15* (7), 3374−3382.
(74) Tahara, K.; O'mahony, M.; Myerson, A. S. Continuous Spherical Crystallization of Albuterol Sulfate with Solvent Recycle System. *Cryst. Growth Des.* **2015**, *15*, 5149−5156.
(75) Steendam, R. R. E.; Keshavarz, L.; Blijlevens, M. A. R.; De Souza, B.; Croker, D. M.; Frawley, P. J. Effects of Scale-Up on the Mechanism and Kinetics of Crystal Nucleation. *Cryst. Growth Des.* **2018**, *18* (9), 5547−5555.
(76) Yerdelen, S.; Yang, Y.; Quon, J. L.; Papageorgiou, C. D.; Mitchell, C.; Houson, I.; Sefcik, J.; Ter Horst, J. H.; Florence, A. J.; Brown, C. J. Machine Learning-Derived Correlations for Scale-Up and Technology Transfer of Primary Nucleation Kinetics. *Cryst. Growth Des.* **2023**, *23* (2), 681−693.

https://doi.org/10.1021/acs.iecr.4c02153
Ind. Eng. Chem. Res. 2024, 63, 18199−18211

(77) Zhao, Y.; Cui, J.; Liu, L.; Hou, G.; Krishna Kamaraju, V.; Glennon, B. Crystal Growth Kinetics of Benzoic Acid in Aqueous Ethanol Solution. *Ind. Eng. Chem. Res.* **2021**, *60*, 1026−1035.
(78) Acevedo, D.; Wu, W.-L.; Yang, X.; Pavurala, N.; Mohammad, A.; O'connor, T. F. Evaluation of Focused Beam Reflectance Measurement (FBRM) for Monitoring and Predicting the Crystal Size of Carbamazepine in Crystallization Processes. *CrystEngcomm* **2021**, *23*, 972.
(79) Yi, Y. J.; Myerson, A. S. Laboratory Scale Batch Crystallization and the Role of Vessel Size. *Chem. Eng. Res. Des.* **2006**, *84* (8 A), 721−728.
(80) Srinivasan, K. Crystal Growth of α and γ Glycine Polymorphs and Their Polymorphic Phase Transformations. *J. Cryst. Growth* **2008**, *311* (1), 156−162.
(81) Kim, S.; Myerson, A. S. Metastable Solution Thermodynamic Properties and Crystal Growth Kinetics. *Ind. Eng. Chem.* **1996**, *35*, 1078.
(82) Su, Q.; Rielly, C. D.; Powell, K. A.; Nagy, Z. K. Mathematical Modelling and Experimental Validation of a Novel Periodic Flow Crystallization Using MSMPR Crystallizers. *AICHE J.* **2017**, *63* (4), 1313−1327.
(83) Busciglio, A.; Montante, G.; Paglianti, A. Flow Field and Homogenization Time Assessment in Continuously-Fed Stirred Tanks. *Chem. Eng. Res. Des.* **2015**, *102* (2008), 42−56.
(84) Alvarez, A. J.; Singh, A.; Myerson, A. S. Crystallization of Cyclosporine in a Multistage Continuous MSMPR Crystallizer. *Cryst. Growth Des.* **2011**, *11* (10), 4392−4400.
(85) Am Ende, D. J.; Am Ende, M. T. *Chemical Engineering in the Pharmaceutical Industry*; Wiley, 2019.
(86) Hadiwinoto, G. D.; Kwok, P. C. L.; Lakerveld, R. A Review on Recent Technologies for the Manufacture of Pulmonary Drugs. *Ther. Delivery* **2018**, *9* (1), 47−70.
(87) Engstrom, J.; Wang, C.; Lai, C.; Sweeney, J. Introduction of a New Scaling Approach for Particle Size Reduction in Toothed Rotor-Stator Wet Mills. *Int. J. Pharm.* **2013**, *456* (2), 261−268.
(88) Variankaval, N.; Cote, A. S.; Doherty, M. F. From Form to Function: Crystallization of Active Pharmaceutical Ingredients. *AICHE J.* **2008**, *54* (7), 1682−1688.
(89) Meenan, P. A.; Anderson, S. R.; Klug, D. L.The Influence of Impurities and Solvents on Crystallization. In *Handbook of Industrial Crystallization*Myerson, A. S.; Erdemir, D.; Lee, A. Y. Eds.; 2002 pp. 67100.
(90) Bourne, J. R.; Zabelka, M. The Influence of Gradual Classification on Continuous Crystallization. *Chem. Eng. Sci.* **1980**, *35* (3), 533−542.
(91) Ejim, L. N.; Yerdelen, S.; McGlone, T.; Onyemelukwe, I.; Johnston, B.; Florence, A. J.; Reis, N. M. A Factorial Approach to Understanding the Effect of Inner Geometry of Baffled Meso-Scale Tubes on Solids Suspension and Axial Dispersion in Continuous, Oscillatory Liquid−Solid Plug Flows. *Chem. Eng. J.* **2017**, *308*, 669−682.
(92) Lide, D. R.; Rumble, J. *Handbook of Chemistry and Physics*, Rumble, J., 103rd ed.; CRC Press, Inc., 2023.

https://doi.org/10.1021/acs.iecr.4c02153
Ind. Eng. Chem. Res. 2024, 63, 18199−18211